CFD simulation of hollow fiber supported NaA zeolite membrane modules

Jiacheng Wang[a], Xuechao Gao[a], Guozhao Ji[b], Xuehong Gu[a],*

[a] *State Key Laboratory of Materials-Oriented Chemical Engineering, College of Chemical Engineering, Nanjing Tech University, 5 Xinmofan Road, Nanjing 210009, PR China*
[b] *School of Environment, Tsinghua University, Beijing 100084, PR China*

A B S T R A C T

NaA zeolite membranes have exhibited excellent performance in pervaporation dehydration of organic solvents. However, the industrial applications based on tubular NaA zeolite membranes are limited due to the high fabrication cost and low permeation flux. Hollow fiber supported zeolite membranes have great advantages of high permeation flux and large packing density, which are beneficial to further reduce the membrane cost. For practical application, it is of great significance to design membrane modules with optimized geometric configuration for the hollow fibers. Here, a hollow fiber membrane module equipped with seven bundles of hollow fiber NaA zeolite membranes and several baffles was designed by computational fluid dynamics (CFD) technique. The effect of baffles on flow field distribution of the membrane module was investigated. The results showed that the membrane module with two radial baffles and four axial baffles not only showed uniform flow distributions inside the module, but also improved the axial velocities along the hollow fibers, which could alleviate concentration polarization. The improved separation efficiency of the membrane module was further confirmed by the experimental characterization.

1. Introduction

Development of efficient separation techniques for organic solvents has been a crucial task in chemical industries. Pervaporation (including vapor permeation) is a promising membrane separation technology with high energy efficiency, which is especially suitable for the separation of azeotropic or close-boiling mixtures [1–6]. NaA membranes with strong hydrophilicities and well-defined micro-pores (0.42 nm), have exhibited extremely high separation selectivity. During the past two decades, NaA zeolite membranes have been industrialized for dehydration of organic solvents [7–15]. Nevertheless, the commercial membrane based on tubular configuration has low permeation flux and packing density in membrane modules, which results in high fabrication cost for membrane facility, thereby restricting its applications in large scales.

To promote the new separation technology, quite a few researchers have turned to develop hollow fiber supported NaA zeolite membranes for dehydration of organic solvents [16–18]. Due to the thin wall thickness and small diameter, hollow fiber supported NaA zeolite membranes provide extremely high permeation fluxes and packing densities in membrane modules. Wang et al. [19] demonstrated that the NaA zeolite membrane supported on α-Al$_2$O$_3$ hollow fiber could provide a high permeation flux up to $9.0\,kg\,m^{-2}\,h^{-1}$ in dehydration of

ethanol/water mixture at 75 °C. Yuan et al. [20] prepared NaA zeolite membranes on a porous seeded α-Al$_2$O$_3$ ceramic hollow fiber via microwave heating method, and showed a maximum selectivity up to 13,000 for ethanol/water mixture at 50 °C. Considering the mechanical strength of hollow fiber zeolite membranes for practical application, our group developed four-channel α-Al$_2$O$_3$ hollow fibers by the combination of phase-inversion and sintering technique [21]. High quality NaA zeolite membranes could be prepared on the external surface of the four-channel α-Al$_2$O$_3$ hollow fiber supports, which exhibited permeation flux of $12.8\,kg\,m^{-2}\,h^{-1}$ for pervaporation dehydration of 90 wt.% ethanol at 75 °C [22]. In order to prepare the four-channel hollow fiber zeolite membranes in batch-scale, an ensemble synthesis strategy was proposed to prepare hollow fiber bundles with membrane area of $0.54\,m^2$ [23]. Such membrane bundles could be further packed together to form an industrial module.

It is important to optimize the geometric configuration of membrane module for improving the uniformity of flow distribution. A comparatively uniform flow distribution can enhance the separation flux of the module [24,25]. Computational fluid dynamics (CFD) method is an ideal tool to explore the flow condition inside the module by analyzing the physical phenomenon, such as flow distribution and heat conduction through the mathematical modeling. So far, many researchers have successfully used CFD method to investigate the flow

---

* Corresponding author.
  E-mail address: xuehonggu@yahoo.com (X. Gu).

Nomenclature

A	effective membrane area (m^2)
$C_{\varepsilon 1}$, $C_{\varepsilon 2}$, C_μ	k-ε turbulence model constant
k	turbulence kinetic energy per unit mass (m^2/s^2)
m	mass of permeate (kg)
N_P	number of planes of the module
n_B	number of elements on the plane of the bundle
n_M	number of elements on the plane of the module
P	static pressure (kg/ms^2)
P_k	shear production of turbulence (kg/ms^3)
S_M	momentum source (kg/m^{2}s^2)
U	velocity magnitude (m/s)
V_{BP}	velocity on the plane of the bundle (m/s)

V_{BPA}	average velocity on the plane of the bundle (m/s)
V_{MA}	average velocity of the whole module (m/s)
V_{MP}	velocity on the plane of the module (m/s)
V_{MPA}	average velocity on the plane of the module (m/s)

Greek letters

ε	turbulence dissipation rate (m^2/s^3)
μ_t	turbulent viscosity (kg/ms)
μ_{eff}	effective viscosity (kg/ms)
ρ	density (kg/m^3)
σ_k	turbulence model constant for the k equation
σ_ε	k-ε turbulence model constant

distribution in the membrane modules. Liu et al. [26] used CFD technique to simulate and optimize the flow field distribution in the modules applied for pervaporation process with different packing densities and cross-section layouts. The optimization of module configuration was achieved, which exhibited a stable flux of $1\,\mathrm{kg\,m^{-2}\,h^{-1}}$ in the acetone-butanol-ethanol fermentation broth during 120 h continuous operation at 40 °C. Zhuang et al. [27–29] developed a novel CFD model to describe the flow field in the shell and lumen sides as well as the filtration process in the porous membrane zone. They concluded that the inlet holes should be evenly distributed at the cross section to achieve uniform flow distribution in the module, and the fractional hole area should be as high as possible to reduce the energy consumption. It would be a good try to use CFD model for the optimization of hollow fiber supported NaA zeolite membranes in dehydration processes.

In this work, we developed a CFD model to investigate the impact of the baffles on separation performance of an industrial-scale hollow fiber NaA membrane modules. We concerned more about the variation of the flow distribution inside the module caused by the baffles. Thus, the

simulation model was set up to describe the flow field in the shell side of hollow fiber membrane module (HFMM). In order to optimize baffle installation, four different structures were selected to make comparisons according to the velocity field and streamline distribution inside the module. The simulation results were also confirmed by the pilot-scale experiments.

2. CFD simulation

2.1. Applied equations

Considering the pressure and temperature of the feedstock in vapor phase are almost unchanged, fluids inside the HFMM for present study can be assumed as ideal, isothermal and continuous in steady state. Because of the fluid colliding against the fiber wall, the fluid was set to be turbulent. The k-ε turbulent model approach, a two-equation turbulence model, was used in this simulation. The first transport variable (k) which is the turbulence kinetic energy, defined as the variance of
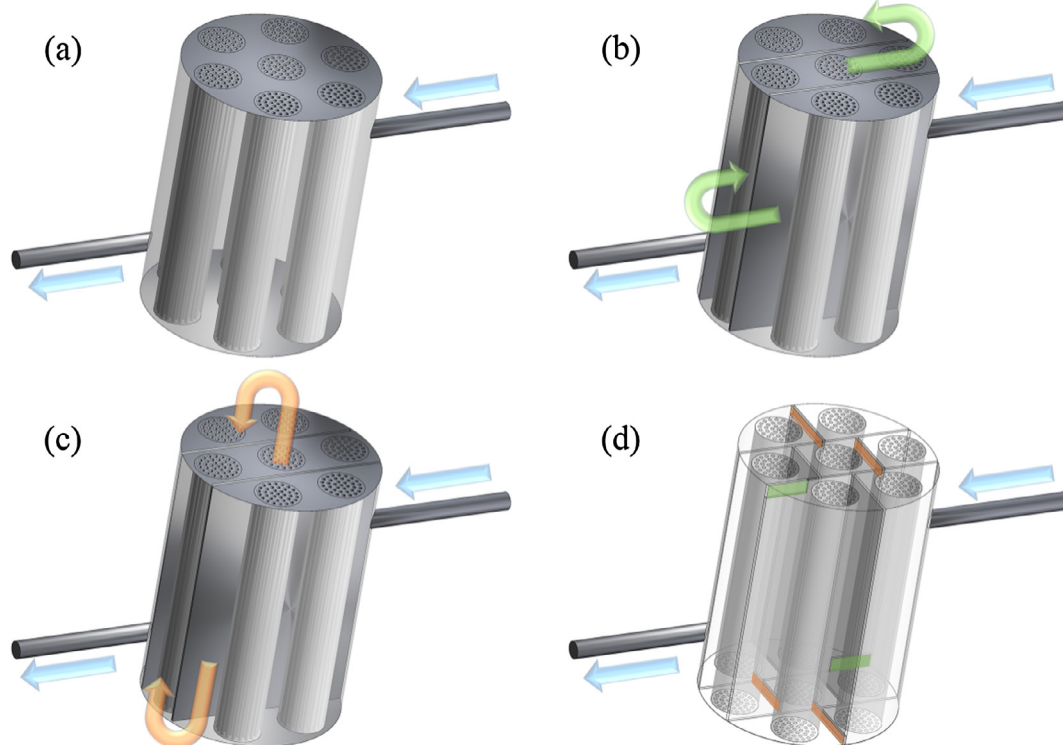

Fig. 1. Structure of the HFMM for CFD simulation, (a) Module 1 (without baffles), (b) Module 2 (equipped with two radial baffles), (c) Module 3 (equipped with two axial baffles), (d) Module 4 (equipped with two radial baffles and four axial baffles).

the fluctuations in velocity. The second transport variable (ε), representing the turbulence eddy dissipation, determines the scale of the turbulence, whereas the first variable, k, determines the energy in the turbulence. Then, the governing equations were modified for k-ε model based on continuity equation, Eq. (1), and Reynolds averaged Navier-Stokes equation for momentum conservation, Eq. (2), respectively, which are expressed as follows:

$$\frac{\partial \rho}{\partial t} + \frac{\partial}{\partial x_j}(\rho U_j) = 0 \tag{1}$$

$$\frac{\partial \rho U_i}{\partial t} + \frac{\partial}{\partial x_j}(\rho U_i U_j) = -\frac{\partial \rho'}{\partial x_i} + \frac{\partial}{\partial x_j}\left[\mu_{eff}\left(\frac{\partial U_i}{\partial x_j} + \frac{\partial U_j}{\partial x_i}\right)\right] + S_M \tag{2}$$

where S_M is the sum of body forces; μ_{eff} is the effective viscosity accounting for turbulence, and p' is the modified pressure, defined as:

$$p' = p + \frac{2}{3}\rho k + \frac{2}{3}\mu_{eff}\frac{\partial U_k}{\partial x_k} \tag{3}$$

The last term in Eq. (3) involves the divergence of velocity, which is neglected in ANSYS CFX. The k-ε model is based on the eddy viscosity concept, so that:

$$\mu_{eff} = \mu + \mu_t \tag{4}$$

where μ_t is the turbulence viscosity. The k-ε model also assumes that the turbulence viscosity is linked to the turbulence kinetic energy and dissipation via the relation:

$$\mu_t = C_\mu \rho \frac{k^2}{\varepsilon} \tag{5}$$

where C_μ is a constant, whose value is 0.09. For the two new variables introduced by the k-ε model, the values can be summarized from the differential transport equations for the turbulence kinetic energy and turbulence dissipation rate:

$$\frac{\partial(\rho k)}{\partial t} + \frac{\partial}{\partial x_j}(\rho U_j k) = \frac{\partial}{\partial x_j}\left[\left(\mu + \frac{\mu_t}{\sigma_k}\right)\frac{\partial k}{\partial x_j}\right] + P_k - \rho \varepsilon \tag{6}$$

$$\frac{\partial(\rho \varepsilon)}{\partial t} + \frac{\partial}{\partial x_j}(\rho U_j \varepsilon) = \frac{\partial}{\partial x_j}\left[\left(\mu + \frac{\mu_t}{\sigma_\varepsilon}\right)\frac{\partial \varepsilon}{\partial x_j}\right] + \frac{\varepsilon}{k}(C_{\varepsilon 1}P_k - C_{\varepsilon 2}\rho \varepsilon) \tag{7}$$

where $C_{\varepsilon 1}$, $C_{\varepsilon 2}$, σ_k and σ_ε are constants with the values of 1.44, 1.92, 1.0 and 1.3, respectively. P_k is the turbulence production caused by viscous forces, which is modeled as:

$$P_k = \mu_t\left(\frac{\partial U_i}{\partial x_j} + \frac{\partial U_j}{\partial x_i}\right)\frac{\partial U_i}{\partial x_j} - \frac{2}{3}\frac{\partial U_k}{\partial x_k}\left(3\mu_t\frac{\partial U_k}{\partial x_k} + \rho k\right) \tag{8}$$

For incompressible fluids, ($\partial U_k/\partial x_k$) is so small that the second term on the right side of Eq. (8) hardly contribute, which becomes

substantial in regions with high velocity divergence for compressible fluids, such as the fluid at shocks in HFMM [30].

2.2. Model geometry and boundary conditions

Industrial HFMM was assumed to be operated in a vapor permeation (VP) process. The HFMM was equipped with seven bundles of hollow fiber NaA zeolite membranes with an area of 1 m^2 for each. Fluid domains in the shell side of the module with the inlet and outlet tubes were created based on the practical module in industrial-scale experiments, as shown in Fig. 1. Computational domain is a cylindrical geometry whose diameter is 220 mm with cylindrical cavities of 4 mm in diameter, representing the lumen side of hollow fibers by Boolean operations. The module body and the hollow fibers are both 300 mm in length, which are supplemented by a standard diameter of 20 mm for the inlet and outlet ports. In this study, four different HFMM structures were investigated. Fig. 1a shows a HFMM without baffles installed (named as Module 1). In Fig. 1b–d, the HFMMs were installed with baffles with different arrangements. For Fig. 1b and c, the radial and axial baffles were installed inside the modules, respectively (named as Module 2 and 3). The baffles in both directions existed in the membrane module were shown in Fig. 1d (named as Module 4).

The model was processed with structured grids of high quality, which was about 17 million elements, so that the computational accuracy was sufficient enough to capture the flow characteristics. The meshing work was done with ANSYS Meshing R 17.1. The method used for meshing ought to obtain high quality mesh and prevent the appearance of skewed nodes and elements. For the whole module, meshing through the construction of hexahedron grids is able to accomplish the meshing automatically. However, the precision of the mesh might not be good enough to achieve the goal of calculation. Thus, the module was divided into a series of blocks to accomplish the meshing, i.e., the parts of membrane units were dealt with fine meshing, while the left parts of the membrane module were meshed in relatively coarse degree. In addition, for the inlet and outlet parts, a combination of hexahedron and wedge grids was used to obtain high quality mesh. Consequently, meshing with individual parts is to prevent the appearance of the flawed grid and save the computing resources. At the intersection face of the two meshing types in different scales, a mesh transition interface was created for numerical data interpolation. The fluid domain for each hollow fiber unit was discretized into about 1.7 million elements, and the number of elements for each unit is nearly the same. Therefore, the precisions for different structures of HFMM are almost identical. Detailed view of the meshing can be seen in Fig. 2.

In all cases, at the inlet port, the magnitude of mass flux was determined as 30 kg/h and the direction of velocity was normal to the boundary. At the outlet port, the boundary condition was set as a static pressure of 1.5 bar. The operation temperature was set as 105 °C for the
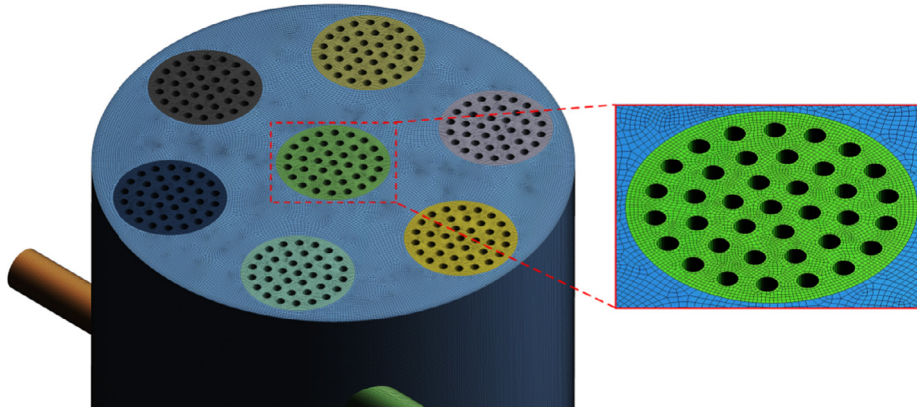

Fig. 2. Meshing geometry with multiblock grids of the hollow fiber for CFD simulation.

entire membrane module. The Reynolds number was calculated more than 10^4 in gaseous under such circumstances, so that the turbulence model was chosen for the turbulent flow. In addition, pure ethanol vapor was chosen as the feed materials during the simulation.

To investigate the performance of the industrial-scale HFMM with CFD method, simplification is needed because of the limitation of the computational resources and the focus of the research. For example, the permeability of the fiber and internal flow inside the fiber can be neglected as this work focused on the shear stress imposed on the outer surface of the fiber [31]. Additionally, due to the insignificant magnitude of permeation velocities of the solute in the direction which is perpendicular to the membrane surface, it is reasonable to assume that permeation velocities have no effect on overall velocity profile [32]. The initial flow distribution at the inlet of the fiber bundle can be treated completely uniform for the study on the effect of the packing density on the axial distribution of flux [33]. A Non-permeable wall function was applied to the membrane walls since the permeate flow for the membrane module can be negligible in comparison with the cross-flow velocity inside the module. Such assumptions can also be found in the relevant literature [26,31], which also simplifies the calculation of the velocity distribution in such large-scale simulation. Ultimately, the CFD simulation mission was accomplished under these conditions.

2.3. Model solution

ANSYS CFX V17.1 was used to solve the turbulent conditions inside the HFMM. The SIMPLE pressure-velocity coupling algorithm, standard-pressure method for pressure calculation, and first-order upwind discretization method for energy, turbulent kinetic energy and dissipation rate were applied to the solution. The default absolute convergence criteria for CFX, 10^{-3} was used for the present solution.

Calculation with two Intel Xenon CPUs and 128 GB of DDR4 RAM was implemented to handle this type of large and sophisticated flow domain for each of the cases. The CFD-Post software package is used for post-processing of the calculation to help to output the optimized result by three dimensions.

3. Experimentation

The NaA zeolite membranes employed in this study were hydrothermally synthesized on the outer surface of seeded α-Al$_2$O$_3$ hollow fiber supports. The pore size distribution, porosity, and tortuosity of the hollow fiber supports were characterized by a mercury porosimeter (PoreMater GT60, Quantachrome Instruments). The mean pore size was measured with a pore-size distribution analyzer (PSDA-20, GaoQ Functional Materials). The detailed preparation of the hollow fiber NaA zeolite membranes was described in our previous work [34]. Considering scale-up of hollow fiber membrane modules, we proposed an ensemble synthesis strategy for preparation of hollow membrane modules [23]. The NaA zeolite membranes employed in this study were hydrothermally synthesized on the outer surface of seeded α-Al$_2$O$_3$ hollow fiber supports, with a diameter of 3.8 mm and a thinnest wall thickness of 0.3 mm. The porosity of the hollow fiber support is approximately 40%, and the pore size is about 200 nm. Experiment has proved that the flux of a single four-channel hollow fiber can achieve 8 kg m^{-2} h^{-1}, and the separation factor was more than 10,000 for separation of water from 90 wt.% ethanol solution at 1.5 bar. The experimental process for VP process in industrial-scale operation is shown as Fig. 3.

Two groups of experiments used for primitive and optimized module were designed respectively, whose VP performances were evaluated by the mixture of 90 wt.% ethanol/water steam. The operating temperature of each group was set as 105 °C. In the VP experiments, ethanol/water mixture was introduced through the outside of the hollow fiber membrane at a gauge pressure of 1.5 bar, while the inside of the hollow fiber was extracted with a vacuum pump, maintained at a downstream pressure below 0.2 kPa throughout the operation. The permeated vapor mixture was collected by the gathering tank through a permeate condenser. The testing time was set to be 6 h for each experiment. The compositions of both feed and permeate were analyzed by a gas chromatography (GC, GC-2014A, Shimadzu) with a thermal conductivity detector and a Porapak Q-packed column. The permeation flux (J_i) of component i toward the hollow fiber NaA zeolite membrane was defined as

$$J_i = \frac{m_i}{A \cdot t} \tag{9}$$

where m_i is the mass of permeate i, kg; A is the effective membrane area, m^2; t is the permeation time, h.

4. Results and discussion

4.1. Velocity contours

Figs. 4–6 depict the velocity contours for the four different structures from three different 2D plane views of the module body. As suggested, all the modules had similar velocity distributions at the inlet because of the constant flow rate set by the inlet boundary condition.
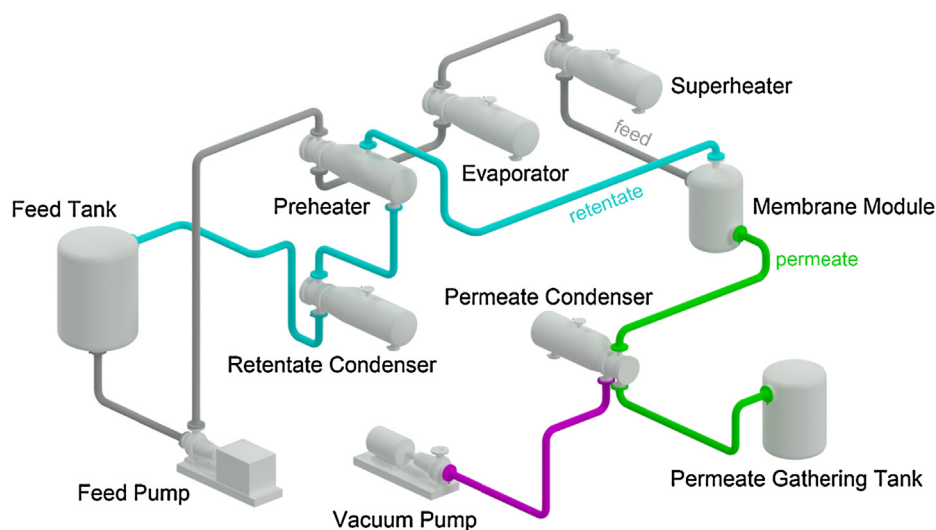

Fig. 3. Schematic diagram of pilot-scale VP dehydration for NaA zeolite membrane.
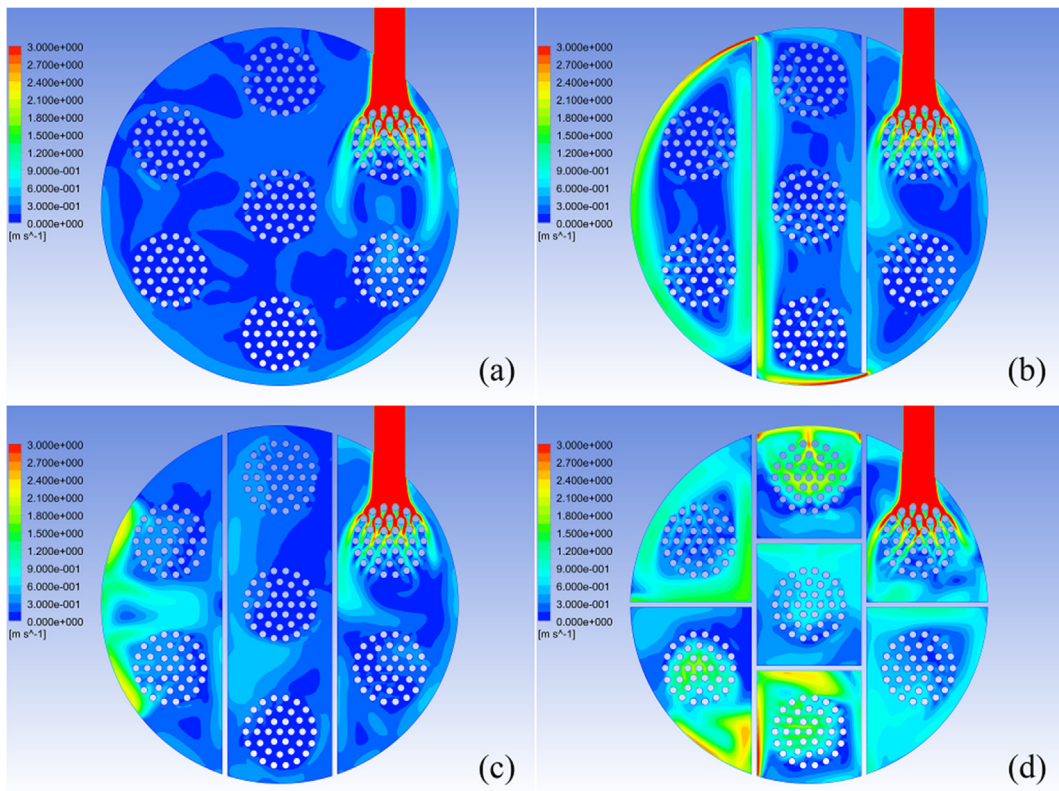
Fig. 4. Velocity contours for HFMM based on the 2D plane on which the inlet tube locates ($Z = 0.05\,\text{m}$), (a) Module 1, (b) Module 2, (c) Module 3, (d) Module 4.
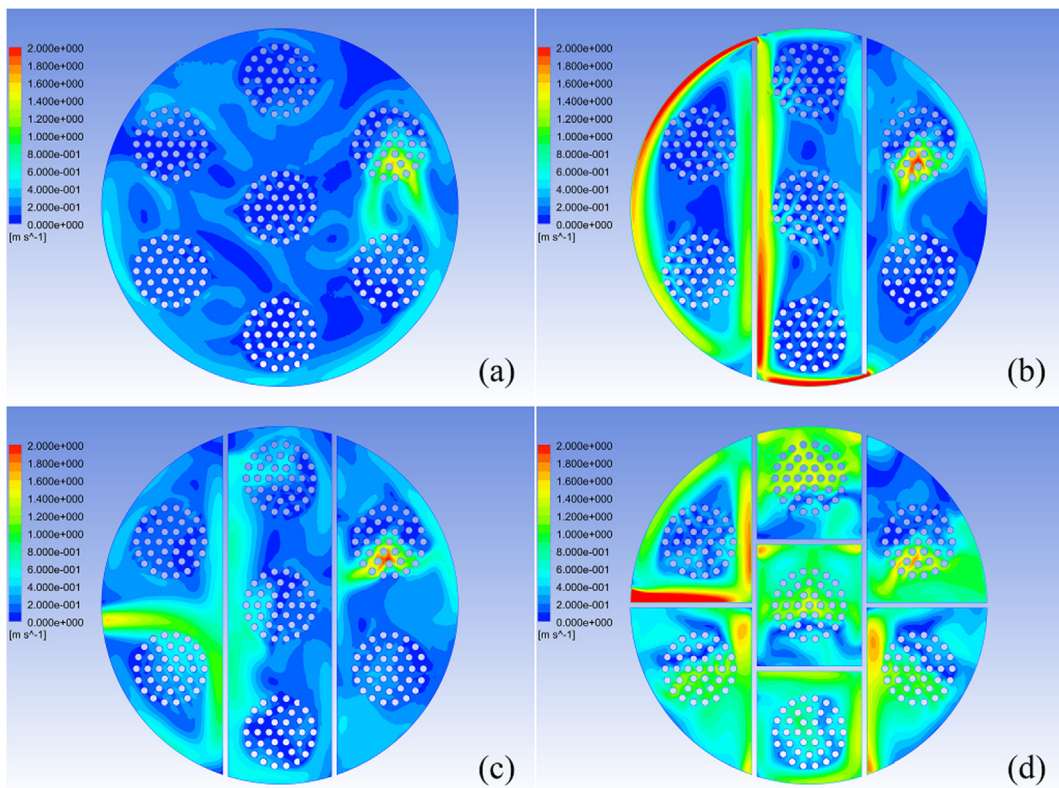

Fig. 5. Velocity contours for HFMM based on the 2D plane of center position ($Z = 0.15\,\text{m}$), (a) Module 1, (b) Module 2, (c) Module 3, (d) Module 4.
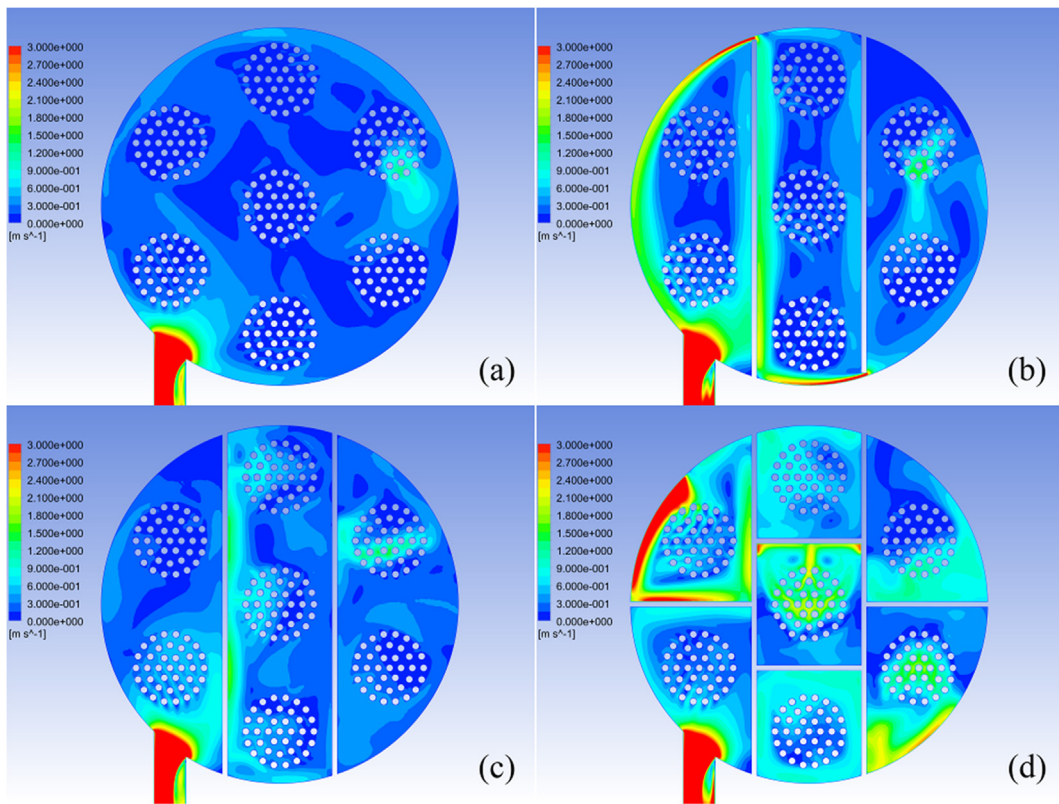
Fig. 6. Velocity contours for HFMM based on the 2D plane on which the outlet tube locates (Z = 0.25 m), (a) Module 1, (b) Module 2, (c) Module 3, (d) Module 4.
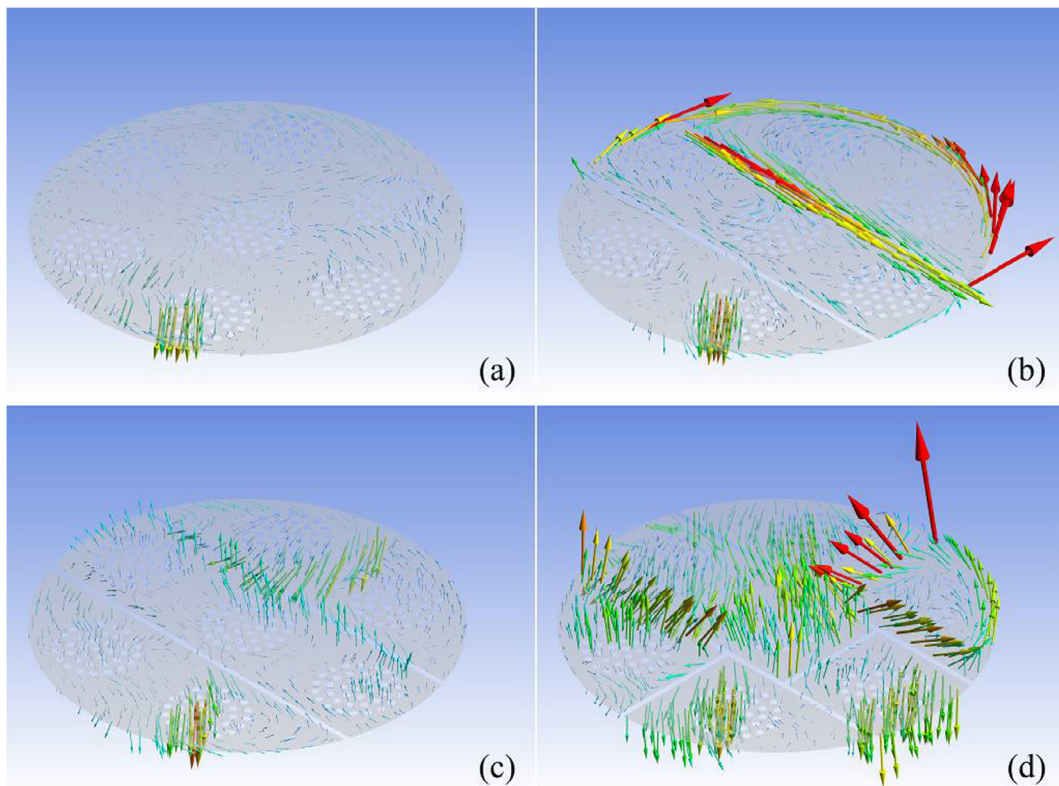

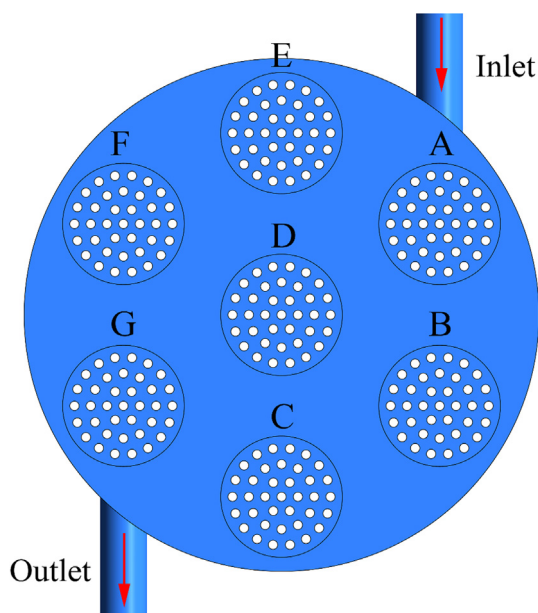**Fig. 7.** Velocity vectors at Z = 0.15 m for the four HFMMs.

Fig. 8. Hollow fiber membrane bundles A-F in the membrane module.

Further, three different base planes were chosen to understand the flow phenomena inside the shell side of HFMM. In Figs. 4 and 6, the obtained cross-sectional views of the flow domain show the velocity contours of the planes on which the inlet and outlet ports locate, respectively. Fig. 5 shows the velocity profile of the section at center position of the module. For Module 1 with no baffles, it is seen that the fluid diffused rapidly at the inlet, forming a high velocity area evidently (Figs. 4a, 5a and 6a). However, the bulk fluid mostly turned into low velocity, which was under 1 m/s. For Module 2, having two radial baffles, the fluid flowed in the radial direction caused by the baffles (Fig. 4b, 5b and 6b). The velocity of the fluid was about 1.5 m/s near the baffles, which was relatively higher than the flow velocity near the hollow fiber bundles. Besides, an extra high velocity area caused by the sudden contraction of the fluid domain occurred in the gap between the module shell and baffles. Compared with Module 1, the velocities near the baffles were enhanced, which facilitates the mass transfer in the module body. For Module 3, having two axial baffles, the phenomenon that the fluid flowed along the radial direction caused by the baffles can be seen (Fig. 4c, 5c and 6c). The velocities near the baffles were also increased, which is similar to Module 2. For Module 4, having two radial baffles and four axial baffles, it is obvious that the velocities in cross sections of each bundle were enhanced significantly (Fig. 4d, 5d and 6d).

Further detailed analysis was conducted on different cross sections. The highest velocity area always occurred in the entrance of the module as given in Fig. 4, which was closely followed by a sudden velocity drop of the flow because of the resistance of hollow fiber bundles. For Module 1, without any baffles, the velocity distribution was uniform, with the velocities of the selected plane bellow 0.6 m/s (Fig. 4a). In Module 2, the fluid motion achieved a speed of 1.8 m/s near the second radial baffle due to the extrusion caused by the three bundles of hollow fibers (Fig. 4b). The resistance of the fiber bundles also resulted in a high velocity area in the outlet part of the module, indicating that some shortcut flow still occurred in Module 2. In addition, a rotational flow also occurred due to the enclosed structure of the outlet part of the module. The appearance of shortcut flow near the baffles can be avoided obviously as seen in Module 3 (Fig. 4c). However, it could be seen that the high velocity region still occurred between two bundles of hollow fibers in the outlet part of the module, due to the short distance between the selected plane and the gap of the baffle. For the middle section of the module, the velocities of the plane were enhanced due to the development of the fluid flow, and the shortcut flow became more

obvious near the baffles in Module 2 (Fig. 5b) and Module 3 (Fig. 5c). Nevertheless, the high velocity area that happened on the upper plane of Module 3 turned to be indistinct on the middle plane, because the middle level is closer to the outlet tube. Additionally, the flow velocities in the hollow fiber units of Module 4 (Fig. 5d) were generally increased, which can promote the mass transfer of pervaporation in the module. For the analysis of the bottom cross section, the high velocity area appeared in the outlet tube of HFMM as Fig. 6 shows. Except for the hollow fiber bundle near the inlet tube, fluids in other units of hollow fibers consistently maintained low velocity for Module 1 and 2, respectively, as shown in Fig. 6a and b. For Module 2, the shortcut phenomenon still existed as the middle section (Fig. 6b), while Module 3 performed better in velocity distribution (Fig. 6c).

4.2. Streamline profile

To further analyze the flow field inside the modules, the velocity vectors profile on the middle plane of the module is given in this section. As shown in Fig. 7, the four graphs represent the velocity vectors at $Z = 0.15$ m of the four different modules, respectively. The direction of the vectors represents the flow direction of the fluid elements, while the length of the vectors illustrates the value of the speed. For Module 1 illustrated by Fig. 7a, most of the streamlines inside the module had relatively low velocities. The central stream of the bundle in the inlet region of the module had a larger velocity than the stream of other bundles, flowing toward the axial direction generally. Moreover, this flow distribution is similar to the streamline profiles of the other structures of HFMM for the bundle near the inlet tube. As shown in Fig. 7b, it is obvious that large number of velocity vectors accumulated near the baffles and the shell of the module near the outlet tube, which indicates that the fast stream impinged on the wall of the shell side and then altered its direction towards the periphery of the module. Although the velocities of these flow vectors were relatively high, the streamlines were mostly developed in radial direction, so that the flow was hard to move along the hollow fibers but would run in a shortcut in great possibilities. By the same method of post-processing for the CFD results, similar phenomena could be found in Module 3 as presented in Fig. 7c. However, the directions of vectors in Module 3 were generally developed along the axis, which were different from the vectors in the module with only radial baffles. Therefore, for the HFMM installed with axial baffles, fluid flow could be affected to re-direct to move along the hollow fibers, which can help the hollow fibers sufficiently contact with the fluid flow. For Module 4 with radial and axial baffles, the flow profile was improved considerably, where the vectors of the section were distributed obviously wider and the velocities of the vectors become higher. As the results illustrated by Fig. 7d, the radial baffles installed in Module 4 can improve the flow ability and facilitate the mass transfer inside the module, and the axial baffles installed in Module 4 help each unit of the hollow fibers contact with the fluid flow in high velocity.

4.3. Flow distribution

The average flow velocities of each cross section of the hollow fiber units are given through CFD simulation. Due to the large number of the grid elements in the CFD model, seven bundles of hollow fibers named by A-G were chosen in the HFMM, as shown in Fig. 8. For the actual operation of HFMM in pervaporation, the velocity and the uniformity of the fluid flow are two important criteria for the design of membrane module. This is because a higher flow velocity inside the hollow fiber units can help the zeolite membrane contacting more feed mixtures, and a more uniform flow can make the membrane layer contact the flow evenly, which finally enhances the permeation flux. The average velocity (V_{BPA}) of the plane for a certain bundle is defined as below.
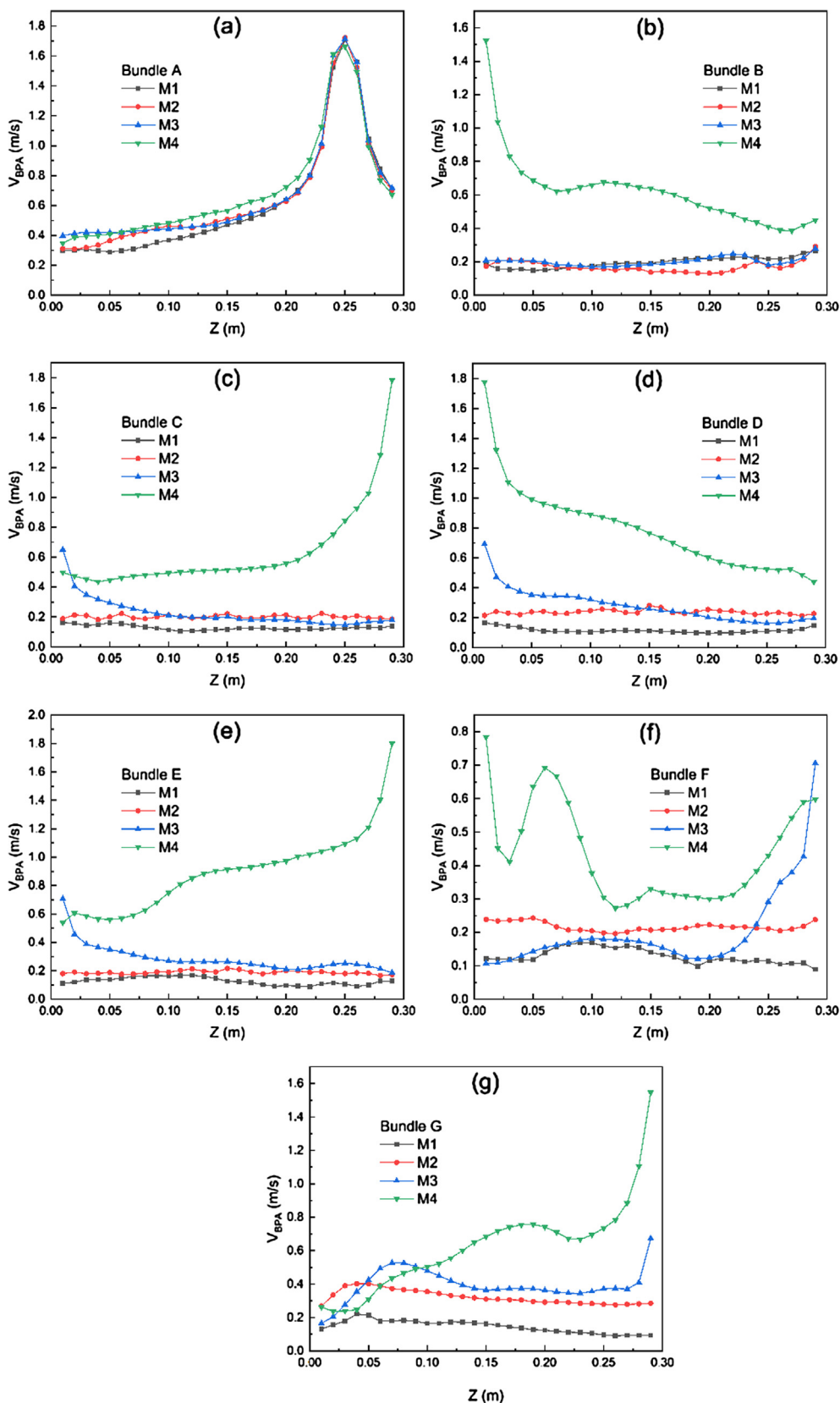
Fig. 9. Average velocity distributions in the seven bundles. (a)-(g) refer to bundles A-G, and M1-M4 refer to Module 1–4.

$$V_{BPA} = \frac{\sum_{i=1}^{n_B} V_{BP,i}}{n_B} \qquad (10)$$

where $V_{BP,i}$ is the velocity of element i on the certain plane of the

bundle, m/s; n_B is the number of elements on the certain plane of the bundle.

Therefore, the variations of the average velocities of each hollow fiber units are illustrated in Fig. 9. As shown in Fig. 9a, all the local

velocities increase significantly at the height range from 0.2 m to 0.25 m along the fiber but decrease sharply for the height above 0.25 m. This is because the inlet tube was installed near the bundle A at the height of 0.25 m. The average velocity changes caused by the module structure are not evident, due to the high momentum of the feedstock from the inlet. However, due to the diversity of the baffle structure, the flux distributions presented in the other bundles significantly vary with module structures. For Module 2, the phenomena that the radial baffles lead to the changes of the flow direction were discussed in the above discussion. In addition, the local velocity distribution is relatively higher than Module 1. At the inlet region, the improvement of the velocity so insignificant that the maximum difference is only 0.1 m/s at a height of 0.07 m in bundle A. Due to the presence of the radial baffles, flowing state was changed, and the local velocity was enhanced, where the maximum difference of the velocities in bundles C-E reached up to 0.11, 0.17 and 0.11 m/s, respectively. Consequently, the largest differences of velocity in bundles F and G were 0.15 and 0.21 m/s. Moreover, the increasing tendency was more stable and significant than the other bundles. For Module 3, it was summarized that the axial baffles may help the fluid run along the hollow fibers. In the inlet region of the module, the flow condition was similar to the case for Module 2, where the promotion is insignificant. However, a regular phenomenon occurred due to the installation of the axial baffles that the velocity profiles in bundles C, D and E were relatively high at the bottom position, while the velocity distributions were obviously higher at the top position for bundles F and G. This is because that the gap formed by the axial baffles is 4 mm in height, so the high velocity area presents for the height below 5 mm. For the bundles in the middle region of HFMM, the velocity difference caused by Module 3 was similar to Module 2 out of the height range of the gap. Nevertheless, the fluid flow velocity for bundle F was unsatisfied as shown in Fig. 9f, for the velocity distribution was nearly unchanged with the axial baffles, while the velocity profile for bundle G was relatively better. Consequently, it is safe to conclude that a shortcut phenomenon occurred in the outlet region of HFMM, as proved by the velocity contours as shown in Figs. 4–6. For Module 4, it is evident to find that the flow velocity inside the unit was enhanced dramatically due to the combination of radial and axial baffles (except for bundle A). As shown in Fig. 9, a regular phenomenon could be found that the high velocity flow existed alternately at the top and bottom of the module, caused by the alternate installation position in axial direction of the baffle gaps, i.e., the high velocity state happened at the top of HFMM as shown in Fig. 9c, e and g, while the high velocity flow existed at the bottom of the module as represented in Fig. 9b, d and f. Unlike the velocity distribution of Module 3, the flow velocities were improved at the whole height of the module, and the velocity increased by nearly 0.5 m/s in bundles D and E.

Moreover, the uniformity of the velocity can illustrate the shortcut flow phenomenon. The average velocity (V_{MPA}) of the plane for the module and the average velocity (V_{MA}) of the whole module are defined respectively as below.

$$V_{MPA} = \frac{\sum_{i=1}^{n_M} V_{MP,i}}{n_M} \tag{11}$$

$$V_{MA} = \frac{\sum_{i=1}^{N_P} V_{MPA,i}}{N_P} \tag{12}$$

where $V_{MP,i}$ is the velocity of element i on the certain plane of the module, m/s; n_M is the number of elements on the certain plane of the module; N_P is the number of planes of the module.

The average velocity of the cross section versus the average velocity of the module represents the uniformity of the flow inside the module, revealing the shortcut flow phenomena inside HFMM. As shown in Fig. 10, it is found that the local fluxes at top of the module were higher than those at the other heights. As shown in Fig. 10, for Module 1–4, the non-dimensional local velocities at the beginning of fiber A were 1.66,

1.35, 1.42 and 1.22 m/s, respectively. This suggested that the uniformity was enhanced obviously because of the baffles. For Module 1, the ratio explained that the uniformity of the velocity distribution largely failed, which might be caused by the occurrences of shortcut flow. For Module 2, the uniformity inside the module was improved a lot, which could be concluded from the red line locating closer to 1. The improving degree of uniformity was relatively low in Module 3, but the trend was smoother than Module 2. In addition, it was found in Module 4 that the flow velocity distribution of HFMM was much more uniform than the other structures as the green line shows.

4.4. Preliminary pilot-scale experiment

To further validate the effect of the installation methods of baffles, a HFMM was equipped with seven bundles of hollow fiber NaA zeolite membranes and baffles as Module 4. A control module without baffles was built for the comparison. The separation performance of the module was evaluated by the VP dehydration of 90 wt.% ethanol/water mixture at 105 °C, where the VP separation results are shown in Fig. 11.

For the primitive module, it was found in the pilot-scale experiment that the water content in permeate maintained at a low level of about 60 wt.% and the flux was approximately $1.3 \, kg \, m^{-2} \, h^{-1}$, so any studies on the flux became meaningless due to the low separation efficiency. The low water content in the permeate side was due to concentration polarization caused by uneven flow distribution, which resulted in more ethanol permeating through zeolite membranes. Experiments were carried out for the optimized module as Module 4 designed. The phenomenon indicated that the module needs some time to stabilize the product flow at approximately $100 \, kg/h$. Overall, the average permeation flux was stable at $1.7 \, kg \, m^{-2} \, h^{-1}$ after 3 h, while the water permeation in permeate became stable at 85 wt.%. The water content of the product was about 2 wt.%. The results suggested improvement of the concentration distribution in Module 4. However, the permeabilities were evidently lower than the results of a single membrane, which could be ascribed to concentration polarity that the concentration distribution was non-uniform and the flow condition inside the module was relatively poor. In a sum, the separation efficiency and the flux could be improved by optimization of module structure in VP process. Further experimental optimization is on-going in our laboratory.

5. Conclusions

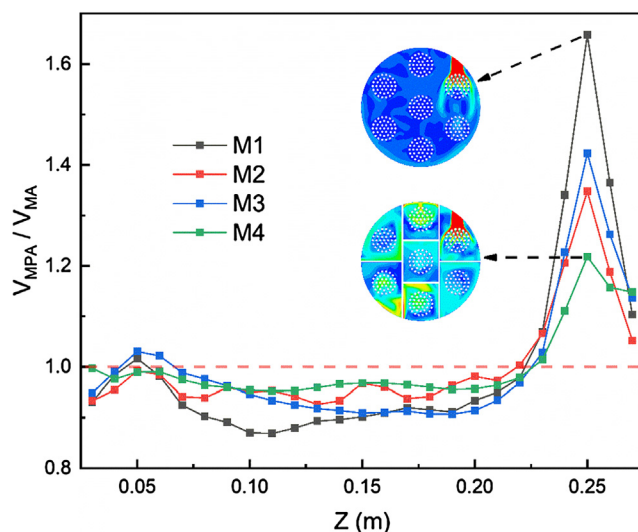The flow inside hollow fiber-supported NaA zeolite membrane

Fig. 10. Flux distributions in the HFMM. M1-M4 refer to Module 1–4.
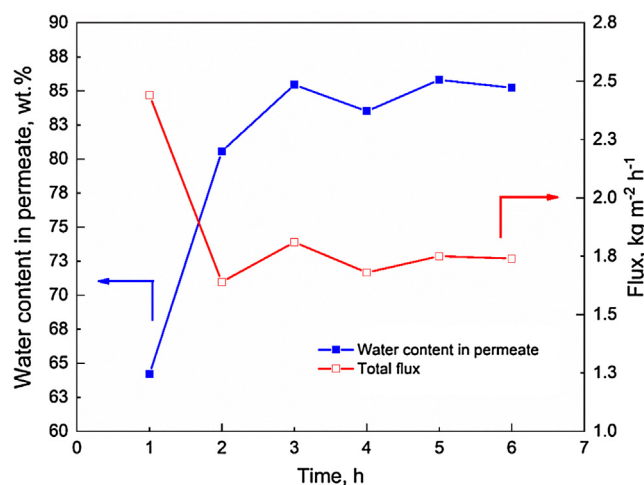
Fig. 11. Time dependence of the performance for the optimized module.

modules was simulated by CFD methods. It is suggested that it is feasible to analyze the velocity distribution and streamline profile inside the module based on the developed CFD model. Simulation results of the four different structures of HFMM were compared. An optimized membrane module structure with two radial baffles and four axial baffles was designed through the comparison among the four different structures, which has relatively high velocities around hollow fiber bundles and uniform flow distribution inside the module. The structure can facilitate the membrane contacting the feed fluid, thereby enhancing the flux of membrane module. In addition, the radial baffles mainly help to optimize the flow direction to ensure that the fluid can flow throughout the entire module; while the installation of the axial baffles can help each bundle contacting with the flow, so that the shortcut can be avoided. The simulation result was also confirmed by the experimental characterization. In the experimental test, the Module 4 showed much higher separation efficiency than Module 1. It can be concluded that the CFD simulation can be applied for the further optimization of hollow fiber-supported NaA zeolite membrane module.

References

[1] X. Feng, R.Y.M. Huang, Liquid separation by membrane pervaporation: a review, Ind. Eng. Chem. Res. 36 (1997) 1048–1066.

[2] W. Yuan, Y.S. Lin, W. Yang, Molecular sieving MFI-type zeolite membranes for pervaporation separation of xylene isomers, J. Am. Chem. Soc. 126 (2004) 4776–4777.

[3] T.C. Bowen, R.D. Noble, J.L. Falconer, Fundamentals and applications of pervaporation through zeolite membranes, J. Membr. Sci. 245 (2004) 1–33.

[4] P.D. Chapman, T. Oliveira, A.G. Livingston, K. Li, Membranes for the dehydration of solvents by pervaporation, J. Membr. Sci. 318 (2008) 5–37.

[5] J. Gascon, F. Kapteijn, B. Zornoza, V. Sebastián, C. Casado, J. Coronas, Practical

[6] approach to zeolitic membranes and coatings: state of the art, opportunities, barriers, and future perspectives, Chem. Mater. 24 (2012) 2829–2844.
C. Zhang, L. Peng, J. Jiang, X. Gu, Mass transfer model, preparation and applications of zeolite membranes for pervaporation dehydration: a review, Chin. J. Chem. Eng. 25 (2017) 1627–1638.

[7] Y. Morigami, M. Kondo, J. Abe, H. Kita, K. Okamoto, The first large-scale pervaporation plant using tubular-type module with zeolite NaA membrane, Sep. Purif. Technol. 25 (2001) 251–260.

[8] J. Caro, M. Noack, Zeolite membranes – Recent developments and progress, Micropor. Mesopor. Mater. 115 (2008) 215–233.

[9] J. Caro, M. Noack, P. Kölsch, Zeolite membranes: from the laboratory scale to technical applications, Adsorption 11 (2005) 215–227.

[10] C. Yu, Y. Liu, G. Chen, X. Gu, W. Xing, Pretreatment of isopropanol solution from pharmaceutical industry and pervaporation dehydration by NaA zeolite membranes, Chin. J. Chem. Eng. 19 (2011) 904–910.

[11] H. Richter, I. Voigt, J.-T. Kühnert, Dewatering of ethanol by pervaporation and vapour permeation with industrial scale NaA-membranes, Desalination 199 (2006) 92–93.

[12] M.P. Pina, R. Mallada, M. Arruebo, M. Urbiztondo, N. Navascués, O. de la Iglesia, J. Santamaria, Zeolite films and membranes. Emerging applications, Micropor. Mesopor. Mater. 144 (2011) 19–27.

[13] B. Bolto, M. Hoang, Z. Xie, A review of water recovery by vapour permeation through membranes, Water Res. 46 (2012) 259–266.

[14] Y.S. Lin, M.C. Duke, Recent progress in polycrystalline zeolite membrane research, Curr. Opin. Chem. Eng. 2 (2013) 209–216.

[15] C. Yu, C. Zhong, Y. Liu, X. Gu, G. Yang, W. Xing, N. Xu, Pervaporation dehydration of ethylene glycol by NaA zeolite membranes, Chem. Eng. Res. Des. 90 (2012) 1372–1380.

[16] A. Huang, W. Yang, J. Liu, Synthesis and pervaporation properties of NaA zeolite membranes prepared with vacuum-assisted method, Sep. Purif. Technol. 56 (2007) 158–167.

[17] X. Shu, X. Wang, Q. Kong, X. Gu, N. Xu, High-flux MFI zeolite membrane supported on YSZ hollow fiber for separation of ethanol/water, Ind. Eng. Chem. Res. 51 (2012) 12073–12080.

[18] X. Wang, Y. Chen, C. Zhang, X. Gu, N. Xu, Preparation and characterization of high-flux T-type zeolite membranes supported on YSZ hollow fibers, J. Membr. Sci. 455 (2014) 294–304.

[19] Z. Wang, Q. Ge, J. Shao, Y. Yan, High performance zeolite LTA pervaporation membranes on ceramic hollow fibers by dipcoating-wiping seed deposition, J. Am. Chem. Soc. 131 (2009) 6910–6911.

[20] W. Yuan, H. Chen, R. Chang, L. Li, Synthesis and characterization of high performance NaA zeolite-polyimide composite membranes on a ceramic hollow fiber by dip-coating deposition, Desalination 273 (2011) 343–351.

[21] Z. Shi, Y. Zhang, C. Cai, C. Zhang, X. Gu, Preparation and characterization of α-Al2O3 hollow fiber membranes with four-channel configuration, Ceram. Int. 41 (2015) 1333–1339.

[22] D. Liu, Y. Zhang, J. Jiang, X. Wang, C. Zhang, X. Gu, High-performance NaA zeolite membranes supported on four-channel ceramic hollow fibers for ethanol dehydration, RSC Adv. 5 (2015) 95866–95871.

[23] M. Ji, X. Gao, X. Wang, Y. Zhang, J. Jiang, X. Gu, An ensemble synthesis strategy for fabrication of hollow fiber T-type zeolite membrane modules, J. Membr. Sci. 563 (2018) 460–469.

[24] T. Akagi, T. Horie, H. Masuda, K. Matsuda, H. Matsumoto, N. Ohmura, Y. Hirata, Improvement of separation performance by fluid motion in the membrane module with a helical baffle, Sep. Purif. Technol. 198 (2018) 52–59.

[25] Y. Liu, G. He, X. Liu, G. Xiao, B. Li, CFD simulations of turbulent flow in baffle-filled membrane tubes, Sep. Purif. Technol. 67 (2009) 14–20.

[26] D. Liu, G. Liu, L. Meng, Z. Dong, K. Huang, W. Jin, Hollow fiber modules with ceramic-supported PDMS composite membranes for pervaporation recovery of bio-butanol, Sep. Purif. Technol. 146 (2015) 24–32.

[27] L. Zhuang, G. Dai, Z.-L. Xu, Three-dimensional simulation of the time-dependent fluid flow and fouling behavior in an industrial hollow fiber membrane module, AIChE J. (2018).

[28] L. Zhuang, H. Guo, G. Dai, Z.-L. Xu, Effect of the inlet manifold on the performance of a hollow fiber membrane module-A CFD study, J. Membr. Sci. 526 (2017) 73–93.

[29] L. Zhuang, H. Guo, P. Wang, G. Dai, Study on the flux distribution in a dead-end outside-in hollow fiber membrane module, J. Membr. Sci. 495 (2015) 372–383.

[30] ANSYS CFX-Solver Theory Guide. Release 17.1, ANSYS Inc., 2016.

[31] R. Kaya, G. Deveci, T. Turken, R. Sengur, S. Guclu, D.Y. Koseoglu-Imer, I. Koyuncu, Analysis of wall shear stress on the outside-in type hollow fiber membrane modules by CFD simulation, Desalination 351 (2014) 109–119.

[32] S. Liu, M. Peng, L. Vane, CFD simulation of effect of baffle on mass transfer in a slit-type pervaporation module, J. Membr. Sci. 265 (2005) 124–136.

[33] J. Günther, P. Schmitz, C. Albasi, C. Lafforgue, A numerical approach to study the impact of packing density on fluid flow distribution in hollow fiber module, J. Membr. Sci. 348 (2010) 277–286.

[34] Y. Liu, X. Wang, Y. Zhang, Y. He, X. Gu, Scale-up of NaA zeolite membranes on α-Al2O3 hollow fibers by a secondary growth method with vacuum seeding, Chin. J. Chem. Eng. 23 (2015) 1114–1122.